Surface & Coatings Technology 494 (2024) 131503

Contents lists available at ScienceDirect

Surface & Coatings Technology

journal homepage: www.elsevier.com/locate/surfcoat

Unleashing the antibiofouling potential of nano-structured ZrN-Cu coating through electricity

José D. Castro [a,*], I. Carvalho [b,c], J.C. Sánchez-López [d], T.C. Rojas [d], R. Escobar-Galindo [e], S. Carvalho [a,f]

[a] CEMMPRE Mechanical Engineering Department, University of Coimbra, 3030-788 Coimbra, Portugal
[b] CEB, Centre of Biological Engineering, LIBRO – Laboratório de Investigação em Biofilmes Rosário Oliveira, University of Minho, Campus of Gualtar, 4710-057 Braga, Portugal
[c] LABBELS–Associate Laboratory, Braga/Guimarães, University of Minho, 4710-057 Braga, Portugal
[d] Instituto de Ciencia de Materiales de Sevilla (ICMS), CSIC-UC, Avda. Américo Vespucio 49, E-41092 Sevilla, Spain
[e] Departamento de Física Aplicada I, Escuela Politécnica Superior, Universidad de Sevilla, Virgen de África 7, Sevilla, 41011, Spain
[f] IPN – LED&MAT – Instituto Pedro Nunes, Laboratório de Ensaios, Desgaste e Materiais, Rua Pedro Nunes, 3030-199 Coimbra, Portugal

ARTICLE INFO

Keywords:
HiPIMS
Maritime
Multifunctional
Antibiofouling
Copper

ABSTRACT

The world needs more environmentally friendly materials every time, especially when the application demands constant interaction with fragile habitats. The naval industry is a crucial player in a globalised economy, and the ambient impact of ships on the seas is well-known. Biofouling is one of the significant issues in this industry, and paints with biocides are used as the principal coating solution. However, those are mechanically poor, releasing heavy pollutants into the oceans. Multifunctional coatings obtained by PVD technology could help overcome this situation. The present study proposes a solution to create an advanced coating composed of zirconium nitride and copper in a specific nano-architecture. The developed coating was obtained in a hybrid magnetron co-sputtering system, employing high-power impulse and direct current power sources in a reactive atmosphere. SEM and TEM expose the morphology and the structure of the coatings. EDX, RBS, and XPS were used to assess the chemical insights of the coating. Halo and biofilm tests (with *Cobetia marina*) were employed to evaluate the antibiofouling action of the coating. The results showed that the activation of the coating, regardless of the used method, provoked the copper migration to the surface, being crucial to obtaining the antibacterial action (reduced bacteria adhesion and $>$ 3 log reduction in CFU on the surface) without affecting the coating integrity (assessed by SEM), and not releasing heavy metals in a significant manner ($<$ 2 log reduction CFU on supernatant). This opens the option of this kind of material, which is environmentally friendly, to be applied in real applications.

1. Introduction

A few factors can stop the world economy, and the naval industry is one of them. Its importance has significantly increased with the rise of globalisation over the years. As the primary mode of transportation for all kinds of goods and merchandise, ships are essential to maintaining our lifestyle and well-being. If ships are affected by problems such as route blockages or malfunctions, operational costs can increase significantly. These increased costs are typically passed directly to the final customers. One of the most common maintenance routines for ships is the removal of biofouling from their external parts. It is well known that biofouling attached to ships can lead to critical problems such as drag increase, which raises fuel consumption and, consequently, pollution. Additionally, biofouling can cause ballast water blockages, potentially affecting the engine cooling system and facilitating the spread of non-indigenous species to different habitats worldwide. Another common problem in ships is corrosion, which degrades the metallic parts exposed to seawater. According to the Association for Materials Protection and Performance (AMPP), formerly the National Association of Corrosion Engineers (NACE), the corrosion phenomena in the marine environment cost around 2.5 trillion USD in 2016 [1]. In this context, such problems are significant issues that the naval industry must address.

It is well known that paints are the most commonly used coatings to avoid the mentioned problems. The main advantages of this technology

* Corresponding author.
E-mail address: jodcastroca@unal.edu.co (J.D. Castro).

https://doi.org/10.1016/j.surfcoat.2024.131503
Received 30 August 2024; Received in revised form 3 October 2024; Accepted 22 October 2024
Available online 28 October 2024

are its ease of application to both small and large areas and its low cost. However, the main drawbacks are their poor mechanical properties and the heavy pollution they cause. The International Maritime Organization (IMO) have started to ban these types of products. For instance, Tributyltin (TBT) paint, which was widely used in this industry to avoid corrosion and biofouling, was banned by the IMO in 2008 [2]. This situation has boosted the search for and development of new solutions, such as nano-texturization [3] or bio-inspired tailored surfaces [4]. Another promising technology for obtaining functionalised surfaces to prevent corrosion and biofouling is Physical Vapor Deposition (PVD), a clean technology with high tailoring capacity [5–7]. He et al. gave an example of a multifunctional coating based on TiO_2/CuO by combining magnetron sputtering technology and annealing treatment. Their results highlighted an achieved biocompatibility, with corrosion resistance and antibacterial ability [8]. Castro et al. obtained a multifunctional coating based on Ag-TiN, which was deposited in 3D ceramic printed substrates and gathered antibacterial ability for decorative purposes [9]. Focussing on the needs of naval industry, reliable mechanical properties, high corrosion resistance and antibacterial/antibiofouling action are the most sought and desired properties in surfaces. Implementing PVD processing oriented towards the naval industry was the subject of the following works; Zhang et al. [10] deposited TiAlCuN coating by magnetron sputtering, showing good erosion-corrosion resistance and antibacterial action against *E. coli;* Zhang et al. [11] developed a mixed coating with graphite-like carbon and Cu clusters using a hybrid magnetron sputtering system with radio frequency and direct current power sources, with a relatively high corrosion resistance and antifouling action. The mentioned examples illustrate how coatings obtained through PVD could effectively address the challenges in the naval industry issues related to corrosion and biofouling.

The sea-chest gratings are critical due to their importance in the good functioning of the ship, avoiding the non-indigenous maritime species transportation worldwide. In this context, this surface must be prepared to resist corrosion, maintaining reliable mechanical properties and being antibacterial/antibiofouling. As the mentioned literature exhibits, the typical approach to get some multifunctionality in PVD coatings for the naval industry is trying to combine ceramic materials, which are reliable in terms of mechanical properties and corrosion resistance, with an active chemical element, which acts as biocidal. The present paper explores the antibacterial/antibiofouling action of a nanostructured coating over metallic specimens commonly used in sea-chest gratings. These were obtained by a hybrid magnetron co-sputtering (MS) system, which employs two different power sources: High power impulse (HiPIMS) and direct current (DCMS). Zirconium nitride is a well-established material which resists corrosion with outstanding mechanical properties for many applications, including machining industries, cutting tools, decorative purposes or diffusional barriers [12]; hence, the implementation under marine environmental conditions is suitable and can contribute to the extension of the lifespan of the coated component and save time reducing the number of maintenance stops. This work builds upon previous studies on zirconium nitride coatings obtained through HiPIMS technology, which demonstrated enhanced mechanical properties (~16 % increase in hardness and ~ 30 % increase in H/E ratio), tribological performance (at least, ~80 % reduction in specific wear rate regardless the contact condition – dry or wet with saline solution) and corrosion resistance (~60 % reduction in corrosion rate), compared to ZrN obtained by DCMS at the same deposition conditions [7,13,14]. The main focus of the present work is explaining how Cu acts as biocide into the ZrN matrix to create a multifunctional coating with antibiofouling properties. The current study will elucidate the performance of the coating in avoiding bacteria attachment and explore the underlying the possible mechanisms responsible for this characteristic. Due to the challenge presented by the biocidal uncontrolled releasing and poor mechanical properties in the current antibiofouling solutions employed by the maritime industry in ships, this work has opted for a dense encapsulation of the biocide (i.e., Cu) as a strategy to mitigate and control this release, trying to keep good mechanical properties and high corrosion resistance and offering an environmentally friendly solution in agreement with the UN SDGs for 2030.

2. Experimental

2.1. Deposition parameters

ZrN-Cu was obtained using a hybrid co-sputtering system equipped with two magnetrons, located 90° apart from the other. Two targets were placed in the magnetrons: Zr (99.9 % purity – Testbourne, 150 × 150 × 8 mm^3 volume) and Cu (99.9 % purity – Testbourne, 150 × 150 × 10 mm^3 volume), which were connected to high-power impulse (HiPIMS - Cyprium™ III plasma generator, Zpulser Inc.) and direct current (DCMS) power sources, respectively. The HiPIMS power source was configured to work in deep oscillation mode (DOMS), and a protective sheet was placed between the magnetrons to avoid cross-contamination during the deposition process. The substrate holder consisted of a metallic tetragon capable of holding until 16 squared substrates, divided into stainless steel 316 L (SS316L – 2 × 2 × 0.1 mm^3) and silicon ⟨100⟩ wafers (Si – 2 × 2 × 0.1 mm^3). As mentioned in previous works [13,15], SS316L was chosen to simulate the material used in the sea-chest gratings, the potential functional part of the present study. The substrate holder is situated in the centre of the deposition chamber at 80 mm distance from the targets. All the substrates were cleaned for 10 min in three different solutions: deionised water, acetone, and ethanol. Before positioning the substrate holder inside the deposition chamber, the cleaned substrates were dried with heated air and glued to this using a conductive silver glue.

The deposition protocol began with a plasma etching process, applying −350 V DC pulsed potential (1.62 μs pulse reverse time and 120 kHz frequency) for 60 min to the substrate holder. Prior to starting, the chamber should reach ~10^{-3} Pa pressure to guarantee the correct working of the plasma deposition process. The etching process was performed in an argon atmosphere (p_{Ar} = 0.3 Pa), and the substrate holder constantly rotated at 23.5 rpm. During this stage, a metallic shield was placed between the substrate holder and the Zr target. The last one was ignited by applying 285 W DC power to remove any potential contamination. Successive to etching, the deposition process begins with the adhesion layer of pure Zr for 400 s (~300 nm thick) in a non-reactive atmosphere (Argon) at 0.4 Pa working pressure and using the HiPIMS power source, which was configured to apply 27 deep sequential oscillations during 1000 μs. The pulse oscillations were set up with 12 μs on-time and 36 μs period. In the course of each oscillation, the current and the potential increase to reach the maximum or peak values (I_p and V_p, respectively) in the on-time and decrease sharply until zero in the off-time (24 μs). The average power and the internal pulse voltage were 1200 W and 300 V, respectively. This configuration allowed us to obtain ~121 kW peak power (P_p), which traduces in ~ −1027 V (V_p) and ~ 118 A (I_p). Secondly, a graded ZrN layer was deposited (~210 nm thick), introducing an increasing N_2 flow into the chamber in four steps of 180 s each and maintaining the target power and the substrate holder rotation speed. In the mentioned steps, the working pressure was kept at 0.4 Pa, and the p_{N2}/p_{Ar} ratio varied as follows: 0.053, 0.111, 0.212 and 0.333. Thirdly, the functional layer deposition starts keeping 0.333 p_{N2}/p_{Ar} ratio and decreasing the rotation speed of the substrate holder in steps of 20 min each. The used rotation speeds were 18, 14, 9, 4 and 2 rpm, obtaining ~1360 nm thick layer (labelled as graded ZrN layer). During Zr and ZrN layer depositions, the metallic shield was placed between the copper target and the substrate holder to avoid cross-contamination. When the substrate holder decreased to 9 rpm, the copper target was ignited, and 25 W DC power was applied to clean it for 60 min. At last, the power in Cu was changed to 190 W, and the metallic shield was removed to start the top layer co-deposition for 840 s (~260 nm thick – labelled as ZrN + Cu layer). Neither bias voltage nor heater were employed along the deposition.

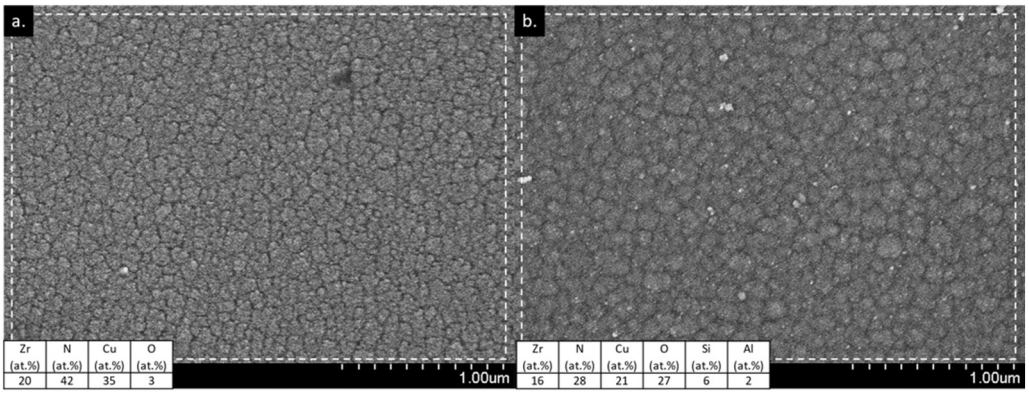

Fig. 1. SEM micrographs and corresponding chemical composition obtained by EDX at 5 kV from (a.) ZrN-Cu and (b.) ZrN-Cu(A) coating surfaces. The enclosed area with dashed lines corresponds to the selected location for the EDX measurement in each sample.

Due to the coating nanoarchitecture, the biocidal agent (Cu) is densely trapped inside the coating (ZrN-Cu). Some samples were chemically activated using a commercial NaOCl solution (5 % *w*/w) to favour the Cu release. These samples (ZrN-Cu(A)) were immersed in this solution for 15 days. Given the biological results, there was also explored an electrochemical activation of the ZrN-Cu samples using a two-electrode cell configuration with the coated sample as a working electrode and carbon (graphite rod) was used as the counter/reference electrode. An electrical potential (−0.5 V vs. graphite electrode) was applied to the working electrodes for 24 h (sample labelled as ZrN-Cu (E)).

2.2. Characterization techniques

Field emission gun scanning electron microscopy (Hitachi S4800 SEM-FEG) and scanning transmission electron microscopy (STEM-FEG—FEI Tecnai G2 F30 S-TWIN) disclosed the coatings' morphology and structure, respectively. STEM-FEG was operated at 300 kV with 0.2 nm point resolution and equipped with a high-angle annular dark field (HAADF) detector from Fischione with a 0.16 nm point resolution. The developed coatings were prepared (from SS316L specimens) in cross-section lamellas utilising a focused ion beam – FIB-FEG-SEM - FEI Helios Nanolab 600i dual beam). The phases present in the coatings were studied by high-resolution transmission electron microscopy (HRTEM). All the post-processing of the obtained micrographs was done in Gatan Digital Micrograph software. Fast Fourier transform (FFT) was employed to get the electron diffraction pattern in a selected area of the HRTEM micrographs. Afterwards, an inverse fast Fourier transform (IFFT) was applied to the pattern, selecting a specific reflection to more precisely determine the selected phase's interplanar spacing (d-spacing). The 'Electron Diffraction tools' script [16] was used in the mentioned post-processing software to reveal the corresponding phases of the diffracting planes.

Elemental chemical composition and the film's chemical distribution were assessed through different characterization techniques. Energy dispersive X-ray spectroscopy (EDX) was conducted using Bruker-X Flash-4010 equipment. High-magnification EDX line profiles were taken from the lamellas in a scanning transmission electron microscope operated at 200 kV (STEM-FEG – FEI Talos F200X). Rutherford backscattering spectroscopy (RBS) was carried out using $^{4+}$He incident ions with an energy beam of 3.5 MeV. The data was processed in the SIMNRA software [17], and the spectra were acquired with a silicon barrier detector located at a backscattering angle of 165°, with an energy detector resolution of 25 keV. X-ray photoelectron spectroscopy (XPS - SPECS Phoibos 150 MCD) spectra were obtained using non-monochromatic Al Kα radiation (1486.6 eV) as an X-ray excitation source and operated at 35 eV pass energy to obtain the high-resolution spectra of the detected elements. The samples were etched with Ar^+ ions (10^{-6} mbar, 2.0 keV and 6 mA) for 5 min to remove superficial contamination (etching rate ≈ 1 Å/min). All the obtained spectra were post-processed in the CasaXPS software, and the electric charge effect was corrected, establishing the main component of the C 1s peak at 285.0 eV.

The antibacterial activity of the developed coatings was tested using *Cobetia marina* DSM 4741 (DSMZ – German collection) cultivated in liquid medium by inoculation of a single colony in 20 mL of Marine broth (MB) 2216 (Merck) at 25 °C and 120 rpm (MB composition: Ammonium nitrate, 1.6 mg/L; Boric acid, 22.0 mg/L; Calcium chloride, 1.8 g/L; Disodium phosphate, 8.0 mg/L; Ferric citrate, 0.1 g/L; Magnesium chloride, 5.9 g/L; Magnesium sulfate, 3.24 g/L; Peptone, 5.0 g/L; Potassium bromide, 0.08 g/L; Potassium chloride, 0.55 g/L; Sodium bicarbonate, 0.16 g/L; Sodium chloride, 19.45 g/L; Sodium fluoride, 2.4 mg/L; Sodium silicate, 4.0 mg/L; Strontium chloride, 34.0 mg/L; Yeast extract, 1.0 g/L). The cellular suspension was adjusted to a final concentration of approximately 1×10^8 CFU/mL, determined by optical density at 620 nm before the halo test and biofouling/biofilm formation assays were used. Zone of inhibition (ZoI) or halo tests adapted from the Kirby-Bauer method were performed according to our previous work [18]. To investigate the biofilm formation, ZrN, ZrN-Cu and ZrN-Cu(A) coatings (previously sterilised at 121 °C for 15 min on both sides) were inoculated with 3 mL of cellular suspension and then incubated at 25 °C under a constant agitation of 120 rpm for 24 h. After incubation of *C. marina*, the coatings were gently washed with phosphate-buffered saline (PBS (1×)) to remove non-attached bacteria. Subsequently, after detaching the adherent bacteria, they were incubated with serial dilutions on MB agar plates at 25 °C for 24 h and then the number of CFU was counted. All the experiments were performed in coated SS316L specimens (including the control sample – ZrN) thrice and independently. Scanning electron microscopy (Hitachi SU3800) was used to study the coating surface after biofilm formation and halo tests without prior deposition of a thin gold layer. Besides, the chemical composition was examined by EDX analysis to disclose any alteration after bacteria/surface interaction. Similar biological assays were also performed on ZrN-Cu(E) coatings. To study the biocide agent release (Cu ions), the ZrN-Cu(E) coatings were immersed in 50 mL of MB at room temperature for 24 h, simulating a seawater exposure. 1.5 mL of solution was removed after 2, 4, 6, 8, 10, 12, and 24 h and studied by inductively coupled plasma optical emission spectroscopy (ICP-OES – ICP PerkinElmer spectrometer model Optima 8000). Results from biological assays were compared using one-way analysis of variance by applying the Dunnett's multiple comparisons test using the GraphPad Prism software. All tests were performed with a confidence level of 99.9 %.

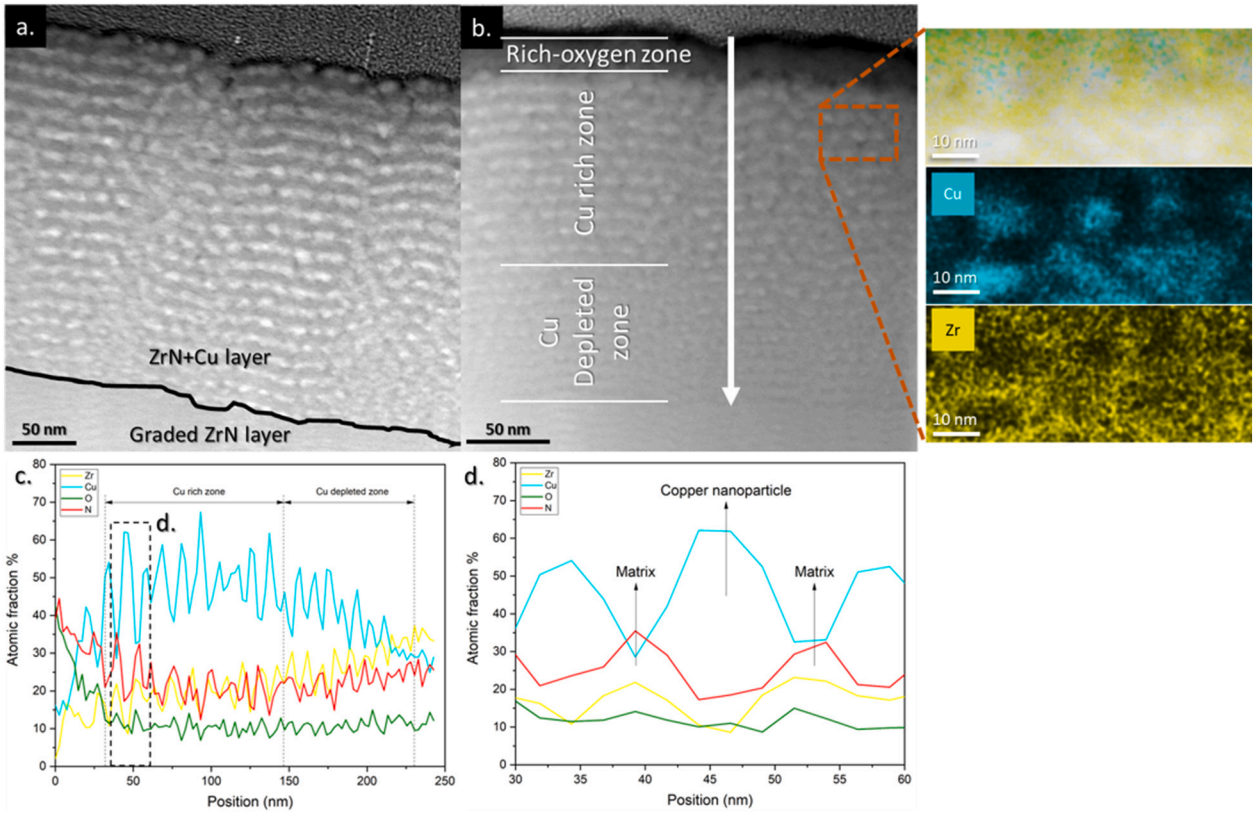

Fig. 2. Cross-section STEM-HAADF images of the top ZrN-Cu functional layer corresponding to the initial state (a.) and, after chemical activation, ZrN-Cu(A) (b.) with a selected enclosed area for elemental mapping. The arrow in (b.) denotes the direction of the EDX profile analysis (c.), and a zoomed analysed area is exposed in (d.).

3. Results and discussion

3.1. Morphological, chemical, and structural features

SEM micrographs show a cauliflower-like morphology of ZrN-Cu and ZrN-Cu(A) (see Fig. 1). The coatings exhibit cauliflower-shaped grains along the surface. The long exposure time to the NaOCl solution seems to provoke a mild enlargement of these "cauliflower" grains in ZrN-Cu(A). Besides, some brighter spots in specific surface points appear after the chemical activation. The chemical composition tables in Fig. 1 suggest that ZrN-Cu(A) suffered an intense oxidation process with a significant copper release. The detection of Si and Al in the chemical composition can be related to feldspars, commonly used in bleaching solutions [19].

The HAADF-STEM micrographs (see Fig. 2), often called *Z*-contrast images, display the nanoarchitecture of the co-sputtered ZrN-Cu layer, formed by alternating Cu-rich and ZrN-rich nanolayers, as shown in the EDX line profile of Fig. 2c and d. The brighter small spots observed in the Cu-rich layers are Cu nanoparticles embedded in ZrN as depicted in the elemental mapping inside the enclosed area (see Fig. 2b). Undoubtedly, the coatings show outstanding compactness, as expected from applying the HiPIMS technology [13]. The hybrid co-sputtering system (HiPIMS + DCMS) in a reactive atmosphere (Ar + N_2) did not modify the film densification in this coating. The chemical composition profile of ZrN-Cu(A) (Fig. 2c) shows how the copper atoms migrated from the deeper zone of the ZrN + Cu layer (labelled as Cu depleted zone in Fig. 2b) towards the surface due to the chemical activation. This fact accounts for the reduction of Cu content shown in the table embedded in Fig. 1 (from 35 to 21 at.%). Another important remark is the strong oxidation in the ZrN-Cu(A) surface (first ~30 nm), which suggests that Zr and Cu could form oxidised species, though this will be discussed later.

SAED digital patterns were obtained after fast Fourier transformation on selected areas of HRTEM micrographs taken in different positions of ZrN-Cu(A): Cu-rich zone (Fig. 3a), Cu-depleted zone (Fig. 3b) and the graded ZrN layer (Fig. 3c). The electron diffraction pattern shown in Fig. 3a exhibits multiple reflections, with the two most intense rings corresponding to the (111) plane of orthorhombic (ort) Zr_3N_4 (d-spacing: 2.97 Å – ICDD no. 51–0646) and the (200) plane of face-centred cubic (fcc) Cu (d-spacing: 2.10 Å – ICDD no. 04–0836). Going deeper into the ZrN + Cu layer, the SAED pattern of the Cu-depleted zone also shows the reflection of the (111) plane of Cu. Additionally, two more reflections were detected and identified as the (111) and (200) of cubic fcc-ZrN phase (d-spacing: 2.64 Å and 2.28 Å, respectively – ICDD no. 35–0753). On the other hand, the SAED pattern in the graded ZrN layer only shows planes corresponding to the fcc-ZrN phase. The (111), (200), (220) and (311) planes were identified with d-spacings 2.64 Å, 2.29 Å, 1.62 Å and 1.38 Å, respectively. The co-existence of fcc-ZrN and ort-Zr_3N_4 phases in the developed coatings is entirely plausible. In previous works, Zr_3N_4 and ZrN phases have always been found simultaneously in the developed coatings [7,13,14]. The orthorhombic Zr_3N_4 phase can be stabilised in ZrN coatings for two reasons: (a.) Oxygen atoms replace nitrogen atoms inside the cubic ZrN lattice, or (b.) oxygen atoms act as a doping agent and promote the Zr_3N_4 presence [7,15,18,20,21]. In this particular case, the exposure to an oxidant solution (NaOCl) increases the oxygen content in ZrN-Cu (as shown in tables embedded in Fig. 1), partially recrystallising the structure to ZrN-oxidised species as Zr_3N_4, which is considered as a poor-doped oxidised nitride. Another possibility for the formation of Zr_3N_4 could be related to the HiPIMS processing, which might increase the inclusion of nitrogen atoms in interstitial sites within the ZrN lattice [13]. As discussed in our previous work, the presence of other oxynitrides species (i.e., Zr_2ON_2 or ZrON) in the obtained coatings is also probable due to the high oxygen content after the chemical activation [7].

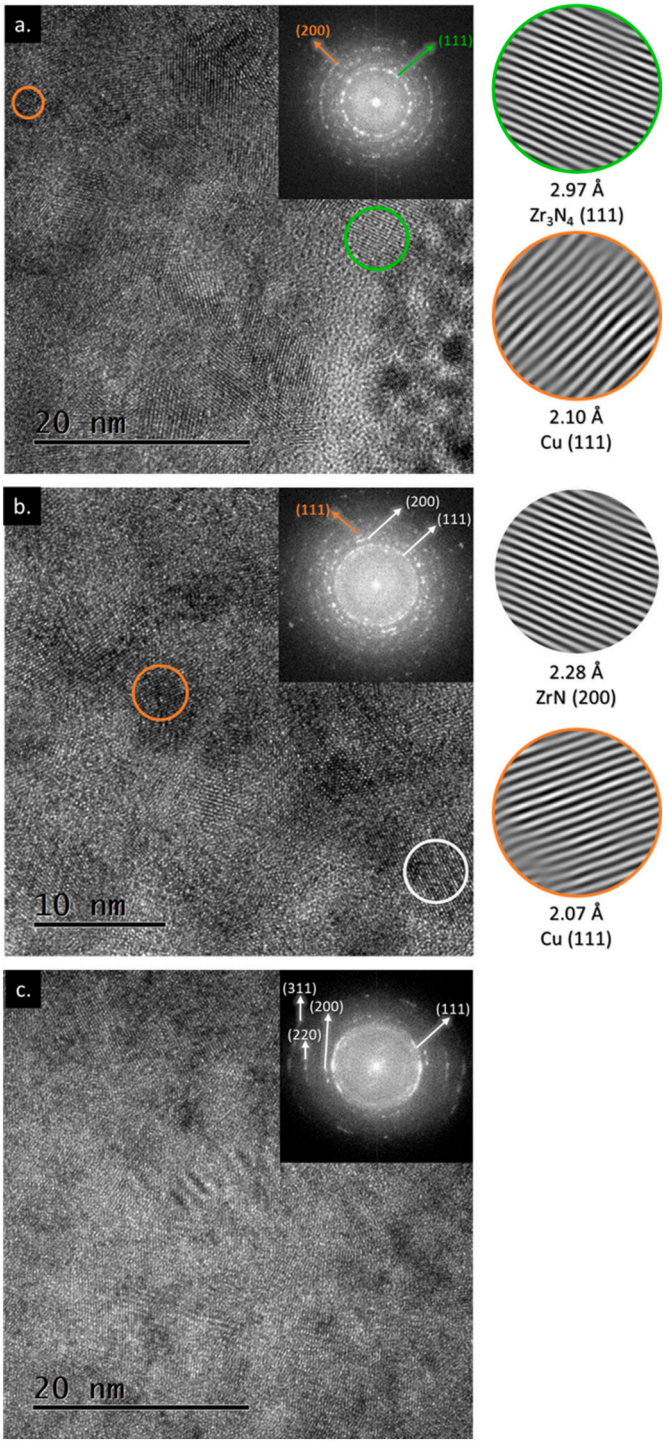

Fig. 3. HRTEM micrographs and SAED patterns in the outermost (a. - inside of the Cu-rich zone in Fig. 2b) and deep (b. - inside of Cu depleted zone in Fig. 2b) parts of the ZrN + Cu layer and the graded ZrN layer (c.) from ZrN-Cu(A).

The RBS spectrum (see Fig. 4) showing the ZrN-Cu(A) composition profile is presented. The contribution of each detected element is exhibited in different colours in the fitted spectrum. On the one hand, the gradual copper profile observed between 2500 and 2750 keV is coherent with the higher concentration of Cu nanoparticles embedded in the top part of the coating, as shown in Fig. 2. On the other hand, the Zr profile (between 3000 and 1500 keV) is coherent with the three-layer stacked deposition performed in this sample: 1) Metallic Zr buffer (1500–2200 keV), 2) graded ZrN layer (represented by a 2-layer stack

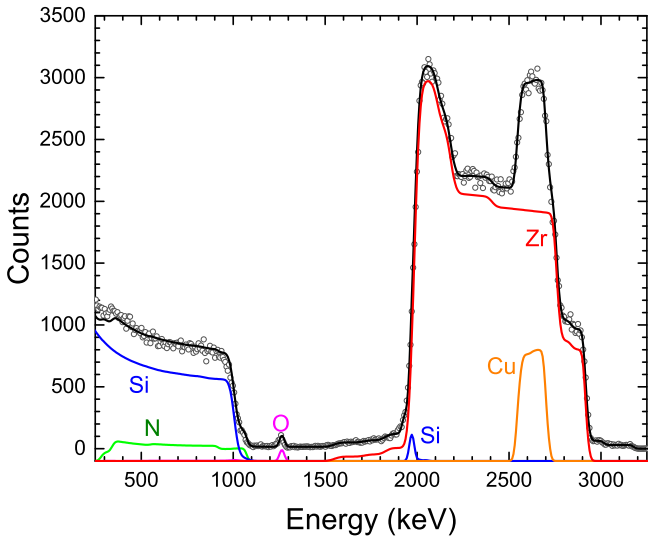

Fig. 4. RBS collected spectrum of ZrN-Cu(A). RBS experimental data (open circles) and the global fitting of results (black solid line) have been shifted vertically from the contributions of the elemental spectra (coloured solid lines in the lower part of the graph) for clarity purposes.

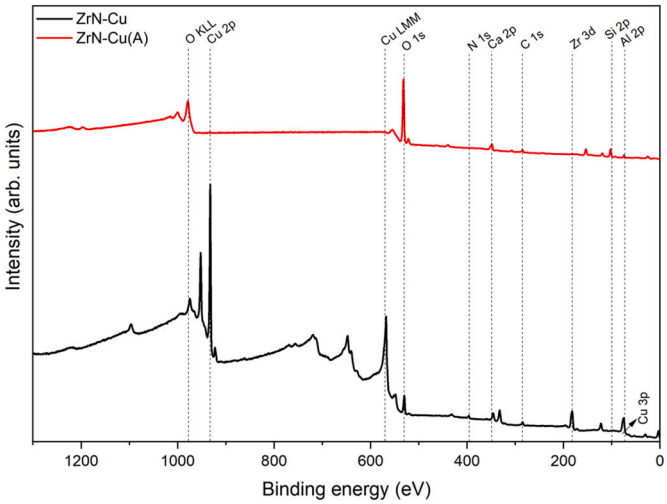

Fig. 5. XPS survey spectra of ZrN-Cu and ZrN-Cu(A) and after 5 min of Ar + bombardment.

composition between 2200 and 2800 keV) and 3) ZrN-Cu layer (2800–3000 keV). The gradual changes observed in the N profile at energies <1000 keV confirmed this elemental depth distribution. Finally, the oxidised top layer displayed in Fig. 2 and in the EDS composition table of Fig. 1, can be confirmed by the sample surface detection of silicon and oxygen RBS signals at ~2000 and ~1275 keV, respectively.

Si and Al detected in the coatings must form part of amorphous phases because none of the SAED patterns revealed the presence of crystalline compounds, including these elements. XPS was performed to demonstrate the chemical bonding states on the coatings' surface, as shown in Fig. 5. The Zr 3d, Cu 2p, N 1s, and O 1s photoelectron peaks corresponding to the ZrN-Cu composition have been identified in the survey spectra. The Ar^+ bombardment helps to reduce the carbon surface contamination layer, thereby improving the signal of the mentioned elements. On the other hand, the ZrN-Cu(A) survey spectrum shows a robust oxidised surface and the presence of Si, Al and Ca, which do not disappear after the etching cleaning process. On the contrary, the Cu 2p

Table 1
Peak parameters detected from ZrN-Cu and ZrN-Cu(A).

Phase/compound	Peak	Binding Energy E_b (eV)	FWHM (eV)
$N\text{-}O_{396}$	N 1s	396.2 ± 0.0	1.8 ± 0.0
ZrN	N 1s	397.7 ± 0.0	2.5 ± 0.0
ZrN	Zr $3d_{5/2}$	180.7 ± 0.0	1.9 ± 0.0
Zr-O	Zr $3d_{5/2}$	181.2 ± 0.0	1.3 ± 0.0
Zr(O,N)	Zr $3d_{5/2}$	181.6 ± 0.0	2.1 ± 0.0
ZrO_2	Zr $3d_{5/2}$	182.2 ± 0.0	2.0 ± 0.0
O^{2-}	O 1s	530.1 ± 0.0	1.8 ± 0.0
Me(O,OH)	O 1s	531.4 ± 0.2	2.8 ± 0.2
SiO_2/Si	O 1s	532.7 ± 0.0	3.0 ± 0.0
Cu + Cu_2O	Cu $2p_{3/2}$	932.6 ± 0.0	1.9 ± 0.0
$Cu(OH)_2$	Cu $2p_{3/2}$	934.5 ± 0.0	2.4 ± 0.0
Plagioclase	Na 1s	1072.1 ± 0.0	2.1 ± 0.0
Plagioclase	Al 2p	74.7 ± 0.0	2.2 ± 0.0
SiO_2/Si	Si 2p	100.1 ± 0.0	1.2 ± 0.0
Plagioclase	Si 2p	102.7 ± 0.0	2.4 ± 0.0
Plagioclase	Ca $2p_{3/2}$	348.3 ± 0.0	2.2 ± 0.0

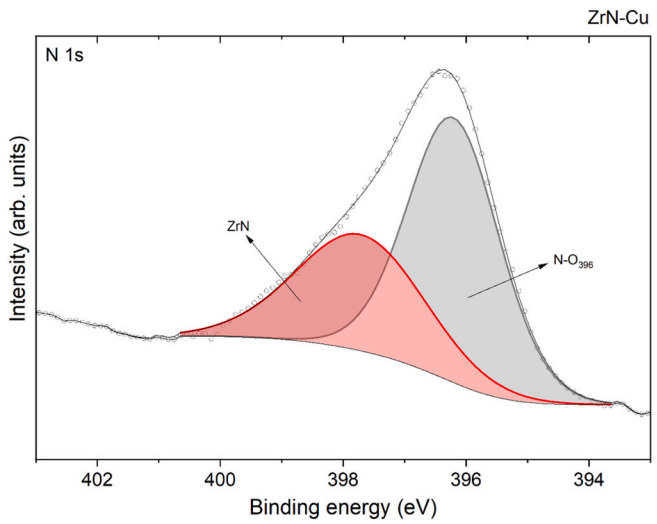

Fig. 6. XPS spectra at N 1s binding level from ZrN-Cu.

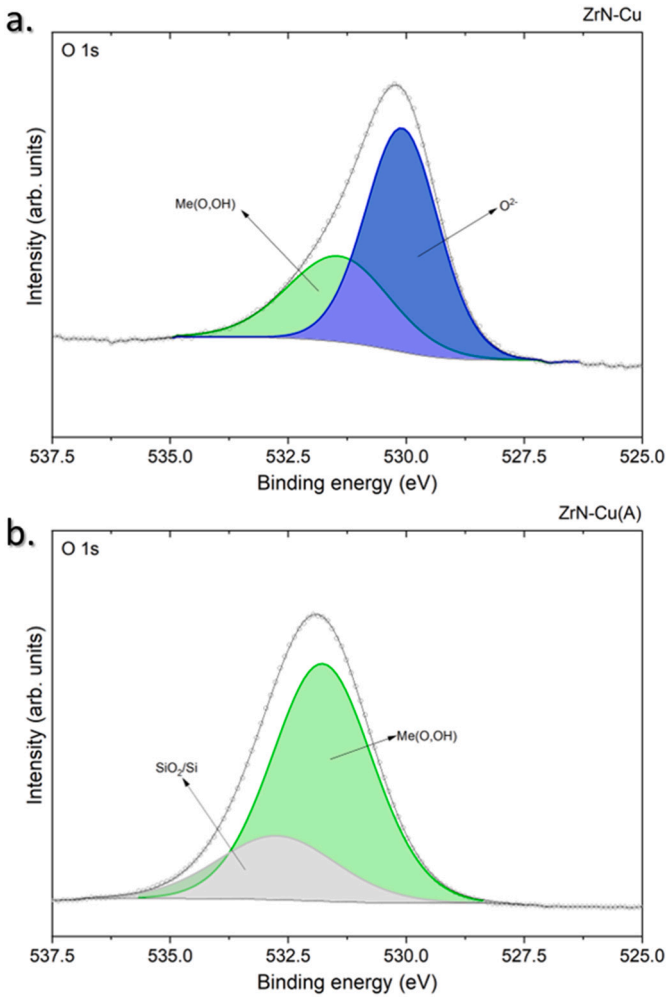

Fig. 7. XPS spectra at O 1s binding level from ZrN-Cu (a.) and ZrN-Cu(A) (b.).

signal was much weaker than the detected one in ZrN-Cu, which disappeared after etching. Another critical remark is that Zr 3d starts to appear after the etching in ZrN-Cu(A). This point will be discussed later, but apparently, the chemical activation of ZrN-Cu has a strong presence of incorporated elements that mask this chemical bond.

In agreement with the coatings' composition, Zr 3d, N 1s, O 1s, and Cu 2p regions were recorded for quantification analysis. Na 1s, Si 2p, Al 2p and Ca 2p spectra were taken exclusively in ZrN-Cu(A). The binding energies of the different photoelectron peaks are summarised in Table 1. Fig. 6 exhibits the N 1s spectrum taken in ZrN-Cu. The same spectrum was taken in ZrN-Cu(A), although the nitrogen signal was not detected, and hence, it confirms the absence of N shown in the survey spectra (see the red spectrum in Fig. 5). After fitting analysis, two components could be distinguished at ~397.4 eV and ~399.0 eV that can be assigned to zirconium nitride and nitrogen-rich oxynitride species, similar to some N 1s peak signals detected in Cu-Zr(*O*)N coatings in a previous work [18].

Fig. 7 exhibits the O 1s spectra for the ZrN-Cu sample before and after NaOCl activation. In the ZrN-Cu sample, two components can be found at 529.6 eV and 531.4 eV, which were attributable to metal oxide/oxynitride and hydroxide phases, respectively, in agreement with our previous works on Cu-Zr(*O*)N and Cu_xO_y sputtered coatings [18,22]. Concerning ZrN-Cu(A), it kept the peak corresponding to Me(O, OH) binding energy and showed an additional peak at ~532.7 eV. According to the literature, this peak is commonly referred to as silicon dioxide/silicon binding, which can be formed after chemical activation and according to the detected elements by EDX in Fig. 1 [23].

Fig. 8 depicts the high-resolution Zr 3d spectra of the developed coatings. Two prominent peaks were detected in ZrN-Cu at ~181.6 eV and ~ 184.0 eV, corresponding to the doublet in 5/2 and 3/2 spin-orbit levels. The binding energy difference between spin orbitals (ΔE_{spin}) in these coatings was ~2.4 eV, in agreement with the reported values in the literature [18]. The peak at ~181.6 eV has been marked as Zr(O,N). Besides, another contribution can be included at lower binding energies corresponding to the Zr—N chemical bonding. This phase is visible at ~179.9 eV. On the other hand, ZrN-Cu(A) shows four peaks corresponding to two Zr doublets. The new peaks at the Zr $3d_{5/2}$ spin-orbit level are localised at ~182.2 eV and ~ 181.2 eV. According to the binding energy values reported in the NIST database and the literature, ZrO_2 is reported between 181.5 eV and 184.0 eV [23,24]. Hence, the peak detected at ~182.2 eV corresponds to this oxide. On the other hand, values ~181 eV commonly are reported as zirconium oxynitrides, though the absence of N in ZrN-Cu(A) discards any presence of these phases. When ZrN is exposed to an oxidising media, it eventually oxidises until it forms ZrO_2, following the route proposed in the literature [18,25]. The no-detection of N in the ZrN-Cu(A) survey spectrum indicates the formation of oxides exclusively on its surface due to the chemical activation process. Based on this, the peak at ~181.2 eV in Fig. 8b could be interpreted as the Zr—O bond signal [24,26]. However, the oxygen-rich media (NaOCl solution) creates an additional outermost layer (see Fig. 2b) in ZrN-Cu(A), containing Si and Al (according to the EDX). ROI spectra of these elements will be studied next.

Fig. 9 exhibits the Cu 2p BEs of ZrN-Cu before chemical activation.

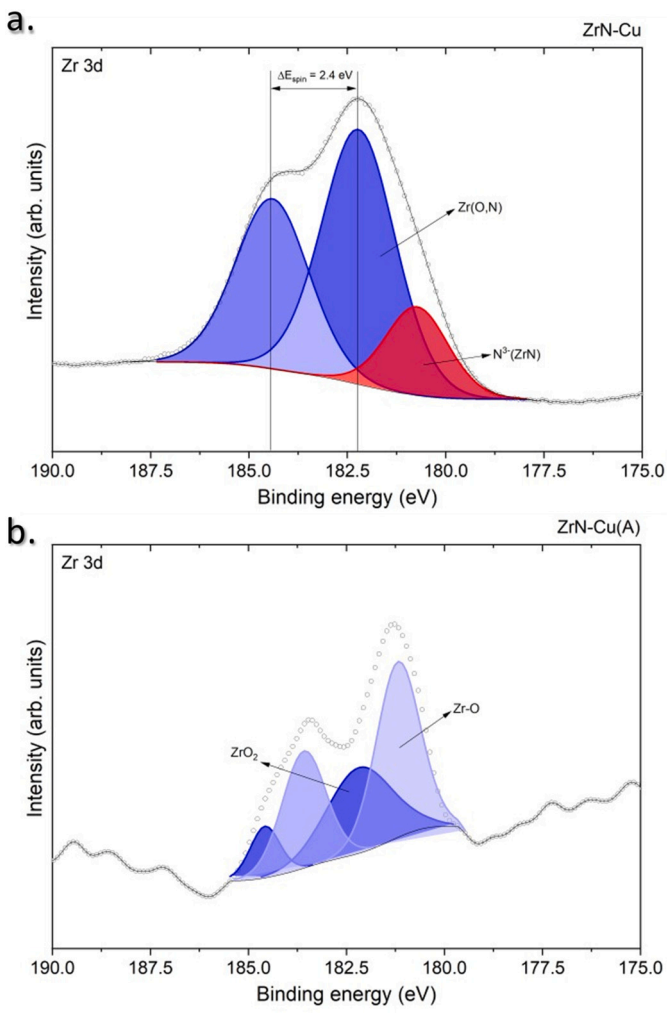

Fig. 8. XPS Zr 3d spectra from ZrN-Cu (a.) and ZrN-Cu(A) (b.).

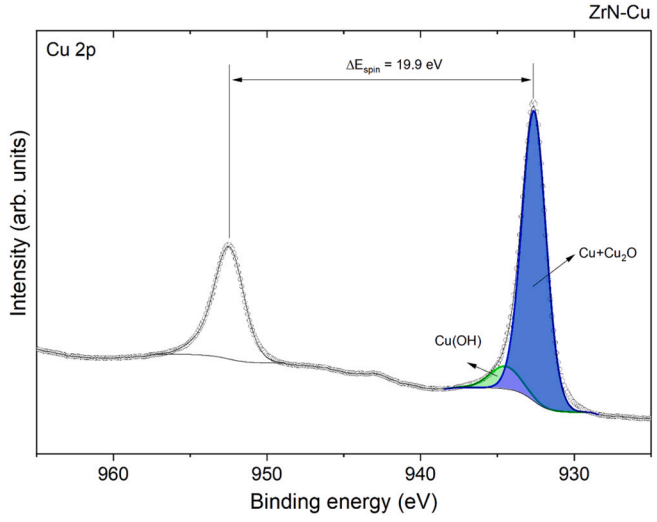

Fig. 9. XPS spectra at Cu 2p binding level from ZrN-Cu.

The sample showed a difference between spin-orbit component energies (i.e., Cu 2p 3/2 and 1/2 spin-orbital positions) around ~19.9 eV, similar to our previous study in Cu_xO_y sputtered coatings [22]. ZrN-Cu spectrum reveals two contributions at the Cu 2p 3/2 spin level around ~932.5 eV

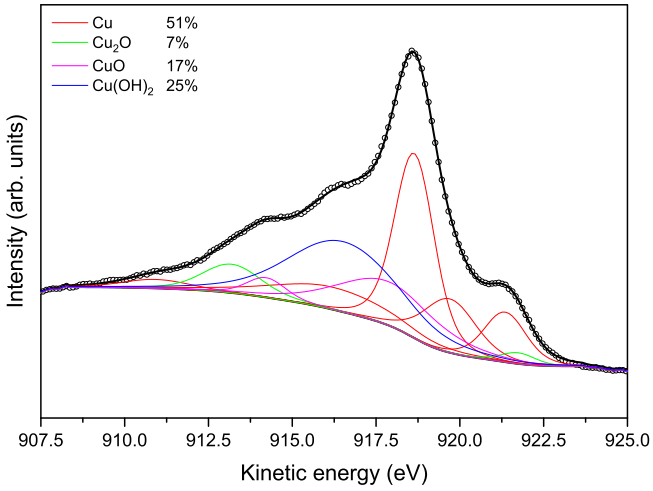

Fig. 10. Cu LMM spectrum of ZrN-Cu with the quantification of Cu anions (at. %).

and ~ 934.5 eV, which correspond to the binding energy of unoxidised copper and Cu_2O (labelled as Cu + Cu_2O) and $Cu(OH)_2$, respectively [18,22]. This last is commonly formed when copper is exposed to ambient conditions [27,28]. This assignment is consistent with the hydroxide signal detected in the O 1s spectrum of etched ZrN-Cu. However, the untouched coatings do not show this bond in the Cu 2p spectra. Concerning ZrN-Cu(A), copper was not detected after the etching process. This is expected according to the exhibited in Fig. 5. However, the XPS spectrum at Cu 2p energy level was taken in ZrN-Cu(A) in an untouched state, revealing a unique peak at ~933.2 eV (see supplementary Fig. SF-1), which corresponds to CuO as the literature reports [27]. The presence of this compound together with the detection of ZrO_2 (see Fig. 8b) in ZrN-Cu(A) confirm that Zr and Cu form superficial oxides due to the strong oxidation during the activation process, as was suggested in the HAADF-STEM micrographs analysis (see Fig. 2). As mentioned in the experimental section, CuO is critical to obtain the antibacterial action. However, the mechanism behind this action will be discussed in the next section [18].

Some authors consider the Cu LMM Auger energy level as applicable to differentiate the copper species due to the proximity among components in the Cu 2p core level [22,27,29]. An additional spectrum was taken in ZrN-Cu in the Cu LMM Auger energy level, as shown in Fig. 10 and the quantification of the Cu anions was performed according to the literature [22,27]. Remarkably, Cu_2O represents 7 at.% in ZrN-Cu, which allows us to conclude that the Cu 2p position corresponds almost exclusively to metallic Cu in Fig. 9. On the other hand, the phases related to the Cu (II) bonding state, represented in the overlapping of Cu $(OH)_2$ and CuO, are constant regardless of the state of ZrN-Cu. This finding suggests the co-existence of these two copper species in ZrN-Cu, which is not clearly defined in the Cu 2p spectrum and explains the origin of the OH^- signal detected in the O 1s spectrum of the ZrN-Cu (labelled as Me(O,OH) in Fig. 7a).

As mentioned, the ZrN-Cu(A) surface shows additional elements due to the chemical activation by bleach solution, including Al, Ca, Na, and Si. The high-resolution XPS spectra of these elements are shown in supplementary Fig. SF-2. The used fitting parameters are reported in the literature and the NIST XPS open database [30,31]. Remarkably, all taken spectra coincided in one unique material, plagioclase (chemical formula - $(Na,Ca)(Si,Al)_3O_8$). Several industries commonly use this feldspar due to its chemical inertness, abundance, and hardness (in the Mohs scale) [32]. As the commercial NaOCl solution formula used for the chemical activation in ZrN-Cu is confidential, it is not very easy to confirm categorically the use of this specific component. However, some scouring products use feldspars in their formula (Bom ami brand -

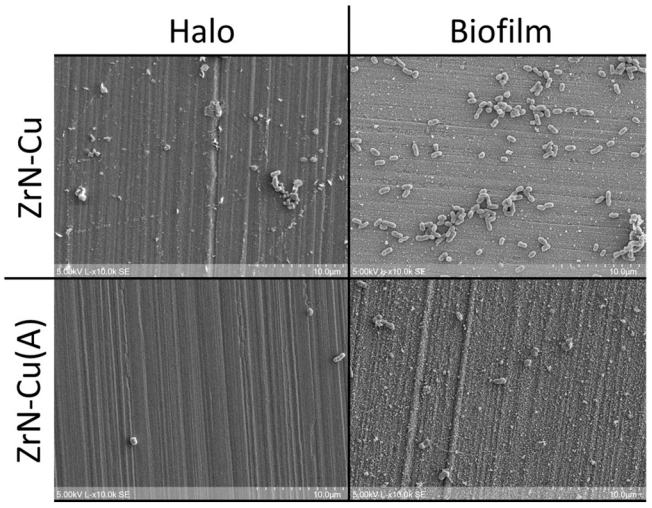

Fig. 11. Superficial SEM micrographs of ZrN-Cu and ZrN-Cu(A) after halo and biofouling/biofilm formation tests.

https://www.bonami.com/products/bon-ami-powder-cleanser/ or Ajax detergent brand – marked as sodium aluminosilicate - https://www.colgatepalmolive.com.au/brands/ajax/ajax-cream-powder/ajax-powder-cleanser). Additionally, the Si 2p spectrum shows a small signal at ~99.87 eV, compatible with the SiO_2-Si bond reported in the literature [33].

Summarising the XPS spectra results, the chemical activation promoted the formation of a top oxide layer comprised of agents present in the bleach solution, and Zr(O,N) originated from the ZrN-Cu film. On the other hand, this process also formed a small amount of CuO on the ZrN-Cu(A) surface, which disappeared with the etching process. This result suggests that this additional layer works as a diffusional layer, controlling the release of copper from the coating. On the other hand, the presence of these chemical species (i.e., CuO and Zr(O,N)) is coherent with the chemical reactions after the activation with the NaOCl solution or after to be exposed to an oxidative electrolyte, which are discussed in our previous works [7,18,22]. As Fig. 2b demonstrates, the copper is not totally released after chemical activation, meaning that this scenario is quite probable.

3.2. Antibacterial and antibiofouling assessment of ZrN-Cu and ZrN-Cu (A)

As mentioned, the antibacterial properties of the samples were assessed by measuring their inhibition zone of bacteria growth, in this case, *Cobetia marina*. This bacteria belongs to aquatic fouling organisms, commonly used to evaluate the antibacterial action of surfaces in marine environments [34–36]. After 24 h of exposure, none of the samples showed a significant halo (a transparent zone free of bacteria) around itself. The tested samples were also checked under SEM, and the obtained micrographs are exhibited in Fig. 11. Undoubtedly, the ZrN-Cu surface shows a higher grade of bacterial attachment than ZrN-Cu(A). This behaviour suggests that ZrN-Cu does not release copper into the surroundings and does not diffuse in sufficient quantities through the MB agar to inhibit bacterial colonisation. In fact, after chemical activation, this coating exhibits minimal bacteria presence on its surface. According to XPS results, copper oxide species are exclusively biocidal agents on samples' surfaces. Notably, ZrN-Cu(A) displayed the signal of CuO, which could significantly influence the bacteria detachment (see supplementary Fig. SF-1). CuO is reported mainly as an effective antibacterial agent, and the results seem to confirm a reduced bacterial colonisation [8,37].

On the other hand, the coatings were also tested in harsh conditions with the same bacteria, favouring the formation of a biofilm over them.

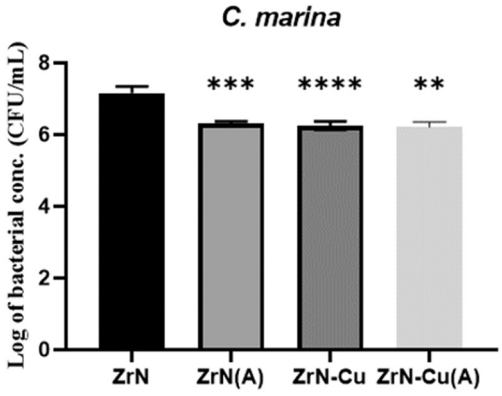

Fig. 12. Logarithmic of microbial concentration after 24 h in contact with *C. marina* of the tested samples: ZrN (control), ZrN(A) (control with chemical activation), ZrN-Cu and ZrN-Cu(A). Asterisks (** $p < 0.01$, *** $p < 0.001$, **** $p < 0.0001$) indicate statistically significant values compared to those obtained from the control (i.e., ZrN).

The results are shown in Fig. 11 demonstrates a clear reduction of bacterial presence in ZrN-Cu(A) compared to ZrN-Cu. This behaviour is coherent with the halo test results (see Fig. 11). After the biofilm formation, the colony-forming units (CFU) were counted to quantitatively check the number of bacteria on the sample's surface. Fig. 12 shows the number of viable cells in terms of the logarithm of bacterial concentration (CFU/mL). Compared to the control sample (i.e., ZrN), the mild reduction (~1 log) of bacteria concentration was statistically significant regardless the sample. According to the Japanese Industrial Standard Z 2801:2000, which establishes a reduction of at least 2 log in bacterial concentration as the threshold for considering a surface to have antibacterial action, none of the samples reached this threshold. The coatings with copper showed a minimal reduction relative to the control sample chemically treated. This confirms that the coatings have a reduced bacterial inhibition exclusively on their surface without showing a significant release of copper towards the surroundings. Still, these cannot be considered antibacterial surfaces.

3.3. Antibacterial and antibiofouling assessment of electrochemical-activated ZrN-Cu

Based on the exposed results, it is clear that copper antibacterial action is limited by the architecture achieved during the deposition. Indeed, the main goal of the developed coating is to present an alternative to create a multifunctional coating that gathers reliable mechanical properties, good corrosion resistance, and controlled antibacterial action. The chemical activation process supplies enough results to differ that the copper inside the coating limits the bacterial adhesion but not enough to be considered an antibacterial surface. An electrical potential was applied to accelerate the copper release and get an effective antibacterial action. The applied potential (−0.5 V vs. graphite electrode) has not been chosen randomly. To determine this, the Pourbaix diagram modelled in our previous work established the possible copper oxide species zones according to pH and applied potential [15]. This study served as a guide to establish the desired reactions in the developed coating without additional undesired responses, which could interfere with the electrochemical activation of the surface, such as oxygen or hydrogen evolution reaction. In the present study, MB (Merck - pH = 7.6 ± 0.2) was used to create the biofilm over the coatings, and it was used as the electrolyte to apply the potential. As mentioned in the experimental section, a graphite rod was used as the counter electrode using the two-electrode cell configuration. A preliminary test was performed for 24 h to establish if the coating released copper successfully without exhibiting corrosion or delamination.

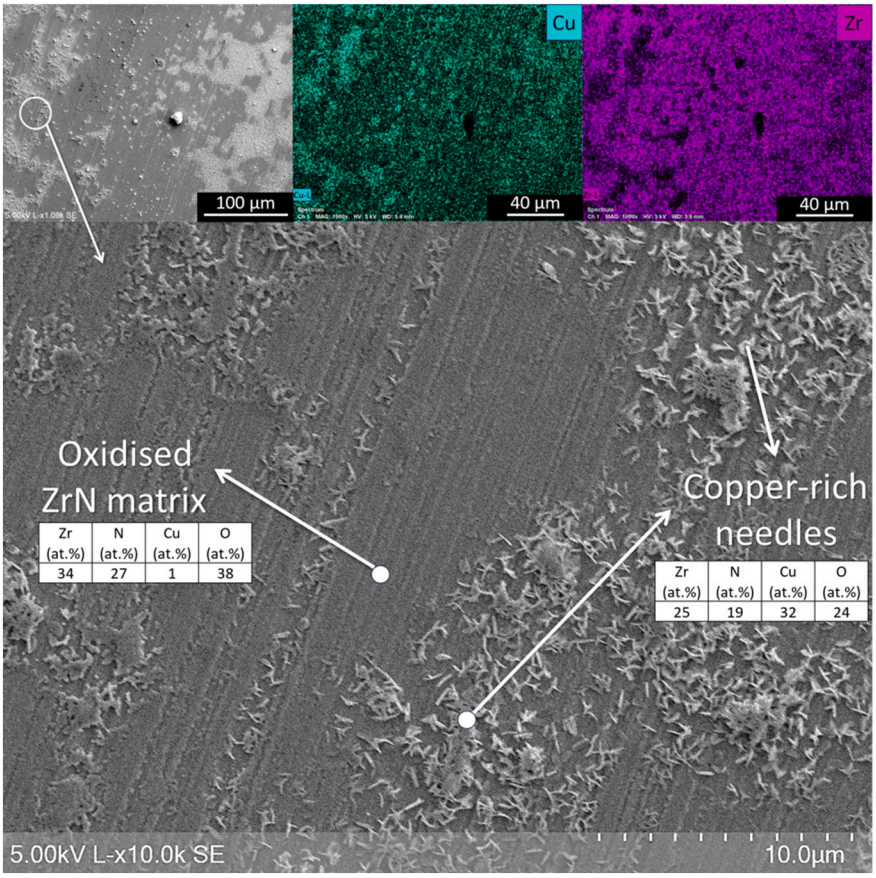

Fig. 13. ZrN-Cu surface after 24 h of electrochemical activation in marine broth with its respective EDX mapping (the green or top-centre image shows the Copper signal and the purple or top-right image shows the Zirconium signal). The filled circles mark the selected areas for the quantification tables obtained at 5 kV. (For interpretation of the references to colour in this figure legend, the reader is referred to the web version of this article.)

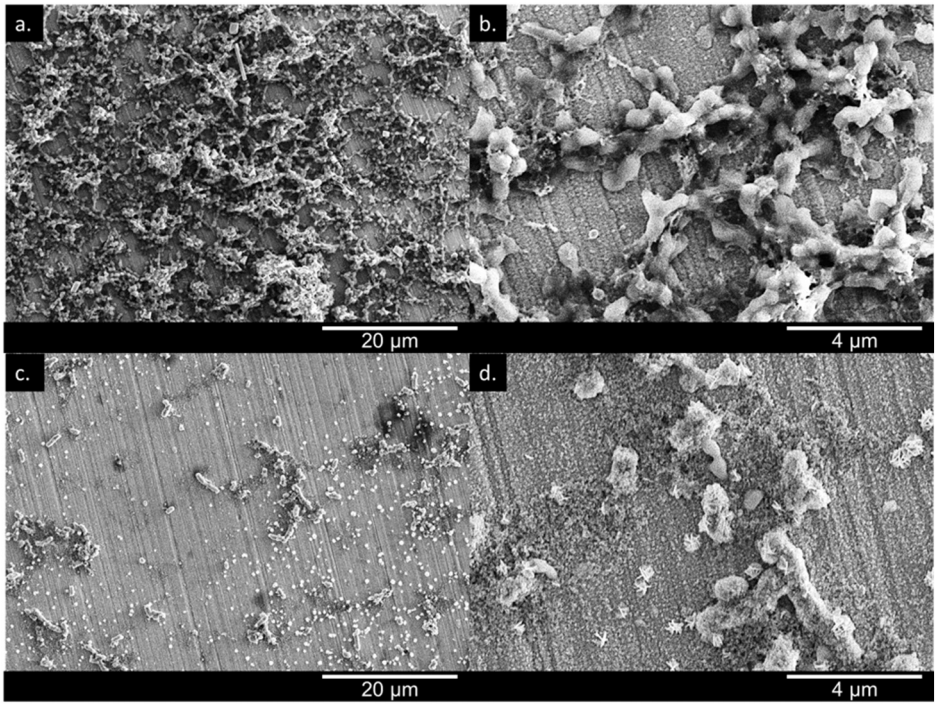

Fig. 14. SEM micrographs of ZrN-Cu (a. & b..) and ZrN-Cu(E) (c. & d.) after biofilm tests.

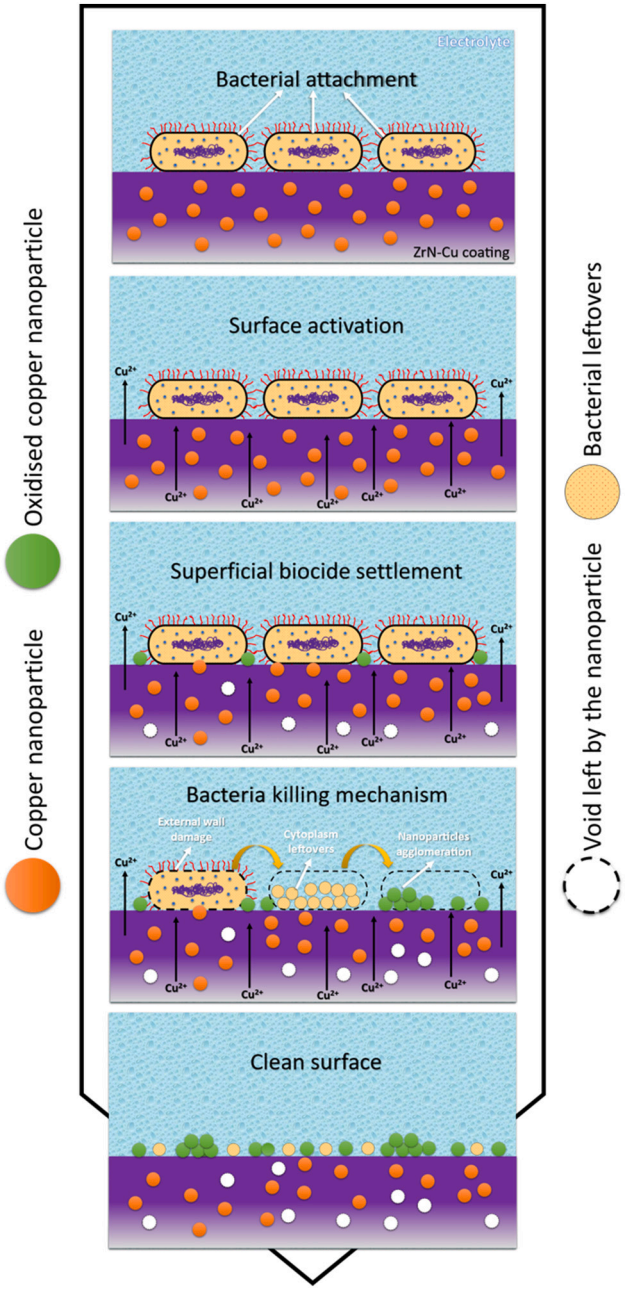

Fig. 15. Schema of surface cleaning in activated ZrN-Cu.

SEM micrographs and EDX mapping were taken in the electrochemically-activated ZrN-Cu sample (labelled as ZrN-Cu(E)); the results are exhibited in Fig. 13. The ZrN-Cu(E) surface displays the formation of needle-like nanoparticles rich in copper on the surface. No delamination or signs of corrosion were observed in SEM micrographs. In fact, according to the Pourbaix diagram of Zr, the formation of ZrO_2 or $Zr(OH)_4$ is possible through the parallel oxidation of the ZrN-Cu surface [38]. In several previous works, this phenomenon was addressed and discussed based on the Gibbs free energy of formation (ΔG_f°) of the possible oxides in this system. Comparing the ΔG_f° values of ZrO_2 ($\Delta G_{f\ ZrO2}^\circ = -1042.8\ kJ/mol$) vs. CuO and Cu_2O oxides ($\Delta G_{f\ Cu2O}^\circ = -146.0\ kJ/mol$; $\Delta G_{f\ CuO}^\circ = -129.7\ kJ/mol$), it is inferred that the formation of ZrO_2 is thermodynamically more favourable than the referred copper oxides [15,22]. The oxygen incorporation during the electrochemical activation probably promotes the creation of a passivation layer aligned with XPS results during chemical activation. None of the additional elements from the electrolyte (i.e., MB) was detected in the EDX mapping, suggesting that the zirconium nitride matrix has been oxidised during this process without any material incorporation (as observed with the activation via NaOCl solution). Besides, the diffusion of copper is more evident than what resulted from the chemical activation (compare Figs. 1b and 13). The diffusion mechanism is possibly similar to the one explained by Calderon Velasco et al. in the ZrCN-Ag system [39], where a passive matrix works as a cathode, and the active nanoparticle works as an anode, hence creating a nano-galvanic coupling and provoking the movement of the active part in the electrochemical cell. An open circuit potential test (see supplementary Fig. SF-3) performed in pure Cu, ZrN and ZrON coatings for 1 h established that Cu is more active (or anodic) than ZrN and ZrON, which makes plausible this mechanism for the diffusion of copper in ZrN-Cu. The high densification obtained due to the HiPIMS processing of ZrN is adequate to encapsulate the copper nanoparticles inside this compound. This grade of densification reduces the zones wherein the coupling between the oxidised ZrN (cathode) and Cu (anode) is possible spontaneously. Hence, employing an external force to provoke the diffusion process is always necessary. Despite the chemical activation promoting the movement of the copper nanoparticles to the surface, this is limited by the scarcity of sinking channels wherein the NaOCl solution could act. Employing electrical potential accelerates this diffusion process significantly, maintaining the integrity of the coating.

Afterwards, the biofilm tests were performed with the same electrochemical activation for 24 h. A ZrN-coated substrate was also tested to check the influence of the electrical potential on biofilm formation. Fig. SF-4 demonstrates that the applied potential does not influence the biofilm growth. On the other hand, Fig. 14 illustrates the significant reduction in bacteria attachment compared to the control sample (ZrN-Cu), which, for this experiment, was the same coating without electrical potential. The new activation process also exhibits how bacteria are eliminated from the surface. Fig. 14d shows bacteria in interaction with some needles and some residues of dissolved bacteria (dusty zones around the bacteria). The copper nanoparticles (needles) interact mechanically with the bacteria, dissolving them until their inner material is disposed of on the coating surface. Besides, some bacteria showed partial degradation, suggesting the antibacterial mechanism still runs on the surface. These micrographs imply that the antibacterial mechanism for ZrN-Cu(E) is the cell lysis mechanism provoked by the copper nanoneedles. According to the literature, the cell membrane is disrupted to expose the cell's inner material (RNA, DNA, protein or organelles) and, consequently, bacteria death [40]. Based on this evidence, Fig. 15 shows a schema of the described bacteria-killing mechanism divided into five stages: (1) The initial bacteria adhesion to the coating surface, (2) the superficial activation, which provokes the copper nanoparticle migration to the coating surface and the releasing of Cu^{2+} to the surroundings, (3) the settlement of the oxidised copper nanoparticles on the surface (as demonstrated in Fig. SF-1), (4) the killing action of the nanoparticles to the attached bacteria/biofilm, provoking their disintegration (cell lysis - see Fig. 14d) with some oxidised nanoparticles agglomeration (see Fig. 13) and finally, (5) a cleaned surface with nanoparticles and bacterial leftovers on it.

Fig. 16 exhibits the results of the CFU concentration counting in the samples' surface and the supernatant marine broth. ZrN-Cu(E) shows a statically significant reduction in CFU, achieving a reduction of ~3.5 log in bacterial concentration compared to ZrN and a ~ 3 log difference with ZrN-Cu. This is substantially different according to the results obtained with the coating activated via NaOCl (i.e., ZrN-Cu(A)), which just shows a reduction in bacterial concentration against ZrN around 1 log and any substantial change when compared to ZrN-Cu (see Fig. 12). Hence, ZrN-Cu(E) accomplishes the standard for being considered an antibacterial surface. An additional bacterial concentration counting was performed in the supernatant media to assess the range of the antibacterial action. Fig. 16b establishes that ZrN-Cu(E) does not possess a significant

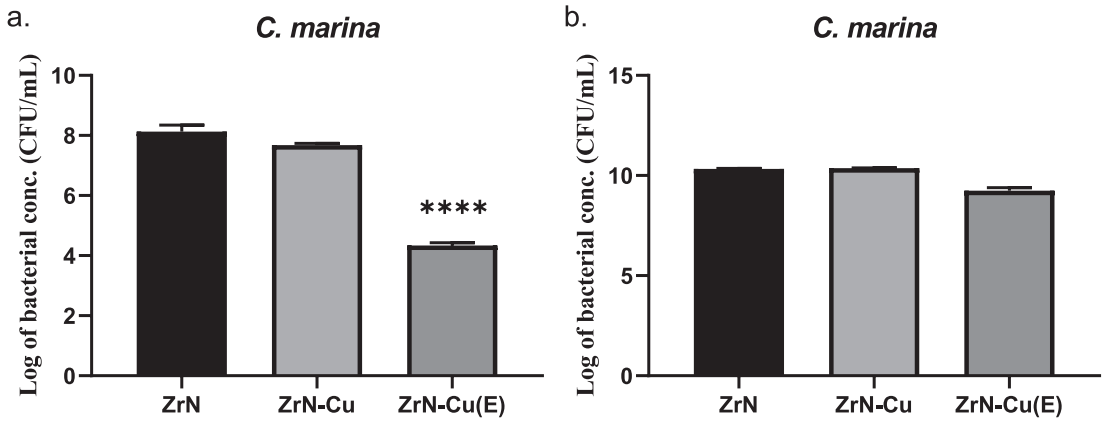

Fig. 16. Logarithmic microbial concentration after 24 h in contact with *C. marina* of the tested samples: ZrN, ZrN-Cu, and ZrN-Cu(E). (a.) represents the counts on the samples' surfaces and (b.) the counts in the supernatant marine broth. Asterisks (**** $p < 0.0001$) indicate statistically significant values compared to those obtained from the control (i.e., ZrN).

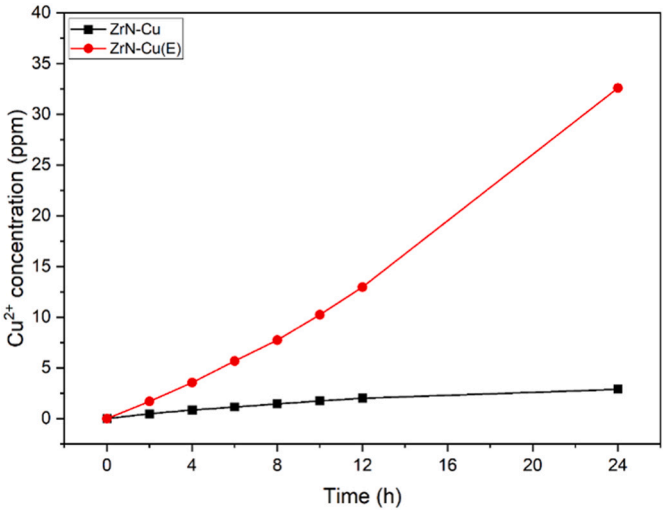

Fig. 17. Cu2+ release along the immersion time of ZrN-Cu and ZrN-Cu(E) determined by ICP-OES.

bactericide effect in the solution, only showing a mild reduction in bacterial concentration (~1 log). These results suggest that the antibacterial action of ZrN-Cu is exclusively by direct contact (as stated in the halo tests – see Fig. 11), and the material released from the coating to the surrounding media is reduced enough not to negatively impact the environment.

Given these results, the release of Cu^{2+} ions from the ZrN-Cu and ZrN-Cu(E) samples into the solution was analysed over 24 h. Fig. 17 shows a progressive increase in the Cu^{2+} concentration in both samples; however, in the electrically activated sample, the release of Cu^{2+} is approximately 11 times higher than that observed for the deposited ZrN-Cu sample. In the case of the electrically activated sample, the release of ions is accompanied by an accumulation of Cu particles on the surface, as observed in the SEM analysis (see Fig. 13). The ZrN-Cu(E) surface shows areas of needle-shaped nanoparticles which are not visible in the deposited ZrN-Cu sample (see Fig. 1a). As explained previously, applying an electrical potential significantly accelerates the process of copper diffusion from the bulk to the coating surface. This result is consistent with the results of the antibacterial tests, which showed that the surface of the ZrN-Cu(E) coating exhibited antibacterial activity. In contrast, the supernatant did not inhibit the growth of planktonic cells despite the high concentration of Cu ions released, demonstrating the antibacterial inactivity of these ions.

According to the ICP results, the copper ion release rate in ZrN-Cu and ZrN-Cu(E) were 19.2 and 217.4 μg/cm^{2}d after 24 h. Some authors report copper ion release rates above 40 μg/cm^{2}d to guarantee an antibiofouling effect [41,42]. Commercial antibiofouling products with Cu can vary from 2 to 66 μg/cm^{2}d, and for instance, the Baltic Sea needs between 2.2 and 5 μg/cm^{2}d to prevent macrofouling [43,44]. However, the evidence presented by this work points to the Cu^{2+} ionic release does not affect the bacteria (i.e., *C. marina*) growing in the supernatant (see Fig. 16b), regardless of the higher copper release rate of the developed coatings compared with the commercial products. As mentioned, the antibiofouling action of the developed coatings is not correlated to the ionic release. Instead, ZrN-Cu had an antibiofouling action due to CuO on the surface and the active Cu nanoparticles' diffusion to destroy the bacteria through the cell lysis mechanism. However, this does not mean the coating does not possess antibiofouling action due to ionic release under real working conditions. The developed surface with fine control of the biocide release rate could represent an interesting option to explore in multifunctional coatings with adaptable antibiofouling action depending on the presented biofouling pressure by any ocean.

4. Conclusion

A novel nano-architecture mixing Zr and Cu, employing a reactive ($Ar + N_2$ atmosphere) hybrid magnetron co-sputtering system composed of high-power impulse and direct current power sources, was obtained. The morphology of the ZrN-Cu coating is cauliflower-like grains, which do not change after the chemical activation with the NaOCl solution. However, this last provokes the migration of copper nanoparticles to the film's surface and the incorporation of additional elements such as Si and Al. The STEM micrographs reveal the high density obtained during the deposition process, a direct consequence of incorporating the HiPIMS processing. Moreover, the nano-architecture of the coating is composed of embedded Cu nanoparticles in a dense ZrN matrix. The electron diffractions expose the co-existence of the ZrN and Zr_3N_4 phases and the presence of the Cu phase.

After activation with NaOCl solution, ZrN-Cu coating exhibits an additional porous top nanolayer composed of amorphous oxides. RBS and XPS establish the existence of SiO_2 and plagioclase, a common component in commercial bleach solutions. Additionally, the Zr 3d spectrum in ZrN-Cu(A) confirms the oxidation of Zr as another consequence of the activation process and the presence of CuO species in the Cu 2p spectrum. According to the Cu LMM Auger XPS spectrum, the Cu^0 state is the most present copper state in ZrN-Cu. This represents an effective encapsulation of the copper nanoparticles without any contamination during the coating manufacturing.

No coating or state (as deposited or chemically activated) showed

antibacterial activity, although SEM micrographs showed reduced bacterial adhesion on ZrN-Cu(A). Copper nanoneedles were observed on the coating surface after electrochemical activation of the ZrN-Cu coating (i.e., ZrN-Cu(E)). These are essential for a multifunctional coating that combines corrosion resistance with antibacterial activity. ZrN-Cu(E) shows a reduction of ~3.5 log in CFU counting, unlike the supernatant, which showed no antibacterial activity with a decrease of ~1 log. In this sense, the antibacterial effect is achieved only on the coating surface by direct contact between Cu and the bacterial cell and not by Cu^{2+} in the surrounding media, reducing the possibility of heavy metal release in the potential application.

The presented solution in the multifunctional coating obtained using a hybrid magnetron sputtering system combining HiPIMS and DCMS technologies and the employment of an electrical potential to control the biocide release rate opens the possibility to explore new options in antibiofouling marine surfaces (especially in sea chest gratings), having total control over the biocidal releasing and offering high adaptability to different biofouling pressure conditions, increasing the efficacy of the antibiofouling action with the minimal environmental impact as possible and far for the antibiofouling commercial paints with minimal biocide release control.

CRediT authorship contribution statement

José D. Castro: Writing – original draft, Visualization, Investigation, Formal analysis. **I. Carvalho:** Writing – review & editing, Validation, Investigation, Formal analysis. **J.C. Sánchez-López:** Writing – review & editing, Validation, Supervision, Resources, Data curation. **T.C. Rojas:** Writing – review & editing, Visualization, Validation, Resources, Data curation. **R. Escobar-Galindo:** Visualization, Formal analysis. **S. Carvalho:** Writing – review & editing, Validation, Supervision, Project administration, Methodology, Funding acquisition, Conceptualization.

Declaration of competing interest

The authors declare that they have no known competing financial interests or personal relationships that could have appeared to influence the work reported in this paper.

Acknowledgements

This research is sponsored by national funds through FCT—Fundação para a Ciência e a Tecnologia, under the PhD Research Scholarship with reference 2020.09436.BD (doi:10.54499/2020.09436.BD) and the doctoral college of Tordesillas (project MO0247) through the University of Coimbra, University of Seville and the Federal University of São Carlos. FEDER Funds funded this research through the program COMPETE - Programa Operacional Factores de Competitividade and by national funds through FCT, under Project No. UIDB/00285/2020 and the program ARISE with reference LA/P/0112/2020. Also, This research is financed by PRR - Recovery and Resilience Plan and by the Next Generation EU Funds, following NOTICE No. 02/C05-i01/2022, Component 5 – Capitalization and Business Innovation - Mobilizing Agendas for Business Innovation under the AM2R project "Mobilizing Agenda for business innovation in the Two Wheels sector" (reference: 7253) and the project DRIVOLUTION (7141 - 02/C05-i01.02/2022.PC644913740-00000022 - 23). Dr. Isabel Carvalho thanks FCT for your contract under the CEEC-Individual — 4th Edition (doi:10.54499/2021.04319.CEECIND/CP1664/CT0010).

Appendix A. Supplementary data

Supplementary data to this article can be found online at https://doi.org/10.1016/j.surfcoat.2024.131503.

Data availability

Data will be made available on request.

References

[1] B. Tuck, E. Watkin, A. Somers, L.L. Machuca, A critical review of marine biofilms on metallic materials, Npj Mater. Degrad. 6 (2022) 25, https://doi.org/10.1038/s41529-022-00234-4.
[2] W.J. Yang, K.-G. Neoh, E.-T. Kang, S.L.-M. Teo, D. Rittschof, Polymer brush coatings for combating marine biofouling, Prog. Polym. Sci. 39 (2014) 1017–1042, https://doi.org/10.1016/j.progpolymsci.2014.02.002.
[3] M. Graham, N. Cady, Nano and microscale topographies for the prevention of bacterial surface fouling, Coatings 4 (2014) 37–59, https://doi.org/10.3390/coatings4010037.
[4] G.D. Bixler, B. Bhushan, Rice and butterfly wing effect inspired low drag and antifouling surfaces: a review, Crit. Rev. Solid State Mater. Sci. 40 (2015) 1–37, https://doi.org/10.1080/10408436.2014.917368.
[5] D. Cavaleiro, D. Figueiredo, C.W. Moura, A. Cavaleiro, S. Carvalho, F. Fernandes, Machining performance of TiSiN(ag) coated tools during dry turning of TiAl6V4 aerospace alloy, Ceram. Int. (2021), https://doi.org/10.1016/j.ceramint.2021.01.021.
[6] J. Antunes, K. Matos, I. Carvalho, S. Carvalho, F. Ferreira, S.M.A. Cruz, Physical vapor deposition Technology in Personal Protective Equipment Production: improved antibacterial and hydrophobic character of textiles, Coatings 12 (2022) 1399, https://doi.org/10.3390/coatings12101399.
[7] J.D. Castro, M. Evaristo, S. Carvalho, Mechanical and anti-corrosion behaviour of ZrNxOy films deposited by reactive high-power impulse magnetron sputtering for maritime applications, Surf. Coatings Technol. 473 (2023) 129991, https://doi.org/10.1016/j.surfcoat.2023.129991.
[8] X. He, G. Zhang, X. Wang, R. Hang, X. Huang, L. Qin, B. Tang, X. Zhang, Biocompatibility, corrosion resistance and antibacterial activity of TiO2/CuO coating on titanium, Ceram. Int. 43 (2017) 16185–16195, https://doi.org/10.1016/j.ceramint.2017.08.196.
[9] J.D. Castro, E. Carneiro, S.M. Marques, B. Figueiredo, A.J. Pontes, Á.M. Sampaio, I. Carvalho, M. Henriques, P.J.S. Cruz, S. Carvalho, Surface functionalization of 3D printed structures: aesthetic and antibiofouling properties, Surf. Coatings Technol. 386 (2020) 125464, https://doi.org/10.1016/j.surfcoat.2020.125464.
[10] X. Zhang, J. Wu, X. Tao, Z. Huang, J. Wang, A. Zammit, C. Tang, J. Chen, Designing Cu chemical distribution in Ti(AlCu)N coatings for enhanced erosion-corrosion and antibacterial performance, Appl. Surf. Sci. 648 (2024) 159053, https://doi.org/10.1016/j.apsusc.2023.159053.
[11] J. Zhang, S. Zhou, Y. Wang, Y. Wang, C. Wang, X. Lu, C. Mao, S. Chen, X. Lu, L. Wang, Enhancing anti-corrosion and antifouling properties of Cu/GLC composite film for marine application, Surf. Coatings Technol. 375 (2019) 414–426, https://doi.org/10.1016/j.surfcoat.2019.07.054.
[12] A. Kumar, R.S. Mulik, Temperature-dependent morphological evaluation of in situ grown hard ZrN coating for enhanced mechanical, wetting and electrochemical properties, J. Mater. Eng. Perform. 33 (2024) 3167–3187, https://doi.org/10.1007/S11665-023-08223-7/FIGURES/14.
[13] J.D. Castro, B. Pinto, F. Ferreira, R. Serra, S. Carvalho, Wettability and corrosion resistance of zirconium nitride films obtained via reactive high-power impulse magnetron sputtering, J. Vac. Sci. Technol. A 41 (2023) 023106, https://doi.org/10.1116/6.0002341.
[14] J.D. Castro, M. Ans, D. Cavaleiro, S. Carvalho, Tribological and mechanical properties of ZrxNy films obtained by HiPIMS in DOMS mode, Tribol. Int. 189 (2023) 108960, https://doi.org/10.1016/j.triboint.2023.108960.
[15] J.D. Castro, M.J. Lima, S. Carvalho, Corrosion resistance of Cu-Zr(O)N films in a simulated seawater environment, Surf. Coatings Technol. 451 (2022) 129050, https://doi.org/10.1016/j.surfcoat.2022.129050.
[16] H. Shi, M. Luo, W. Wang, y, Comput. Phys. Commun. 243 (2019) 166–173, https://doi.org/10.1016/j.cpc.2019.04.012.
[17] M. Mayer, SIMNRA 7.03, (n.d.). https://mam.home.ipp.mpg.de/ (accessed June 27, 2024).
[18] J.D. Castro, M.J. Lima, I. Carvalho, M. Henriques, S. Carvalho, Cu oxidation mechanism on cu-Zr(O)N coatings: role on functional properties, Appl. Surf. Sci. 555 (2021), https://doi.org/10.1016/j.apsusc.2021.149704.
[19] R. Cañedo-Mondragón, P. Eguía-Aguilar, M. Pérezpeña-Díazconti, F. Arenas-Huertero, Identification of ferruginous bodies in the lungs of children and analyses of the elemental composition of fibers, Inhal. Toxicol. 25 (2013) 517–524, https://doi.org/10.3109/08958378.2013.808288.
[20] P. Carvalho, F. Vaz, L. Rebouta, L. Cunha, C.J. Tavares, C. Moura, E. Alves, A. Cavaleiro, P. Goudeau, E. Le Bourhis, J.P. Rivìre, J.F. Pierson, O. Banakh, Structural, electrical, optical, and mechanical characterizations of decorative ZrOxNy thin films, J. Appl. Phys. 98 (2005), https://doi.org/10.1063/1.1990261.
[21] C. Moura, P. Carvalho, F. Vaz, L. Cunha, E. Alves, Raman spectra and structural analysis in ZrOxNy thin films, Thin Solid Films 515 (2006) 1132–1137, https://doi.org/10.1016/j.tsf.2006.07.039.
[22] J.D. Castro, M.J. Lima, S. Carvalho, Wetting and corrosion properties of CuxOy films deposited by magnetron sputtering for maritime applications, Appl. Surf. Sci. 584 (2022), https://doi.org/10.1016/j.apsusc.2022.152582.
[23] NIST X-ray Photoelectron Spectroscopy Database, (n.d.). https://srdata.nist.gov/xps/ (accessed June 4, 2024).

[24] H.S.P. Vanegas, S.V. Calderon, J.E.O. Alfonso, J.J.F. Olaya, P.J. Ferreira, S. Carvalho, Influence of silicon on the microstructure and the chemical properties of nanostructured ZrN-Si coatings deposited by means of pulsed-DC reactive magnetron sputtering, Appl. Surf. Sci. 481 (2019) 1249–1259, https://doi.org/10.1016/j.apsusc.2019.03.128.
[25] T. Mishima, M. Matsuda, M. Miyake, Visible-light photocatalytic properties and electronic structure of Zr-based oxynitride, Zr2ON2, derived from nitridation of ZrO2, Appl. Catal. Gen. 324 (2007) 77–82, https://doi.org/10.1016/j.apcata.2007.03.017.
[26] D. Cristea, A.I. Scărlătescu, C. Croitoru, A. Marin, I.L. Velicu, V. Tiron, D. Martínez-Martínez, C.I.D.S. Oliveira, L. Cunha, Photocatalytical and corrosion behavior of sputtered zirconium oxynitride thin films doped with titanium, Surfaces and Interfaces. 42 (2023), https://doi.org/10.1016/j.surfin.2023.103488.
[27] M.C. Biesinger, Advanced analysis of copper X-ray photoelectron spectra, Surf. Interface Anal. 49 (2017) 1325–1334, https://doi.org/10.1002/sia.6239.
[28] I. Platzman, R. Brener, H. Haick, R. Tannenbaum, Oxidation of polycrystalline copper thin films at ambient conditions, J. Phys. Chem. C 112 (2008) 1101–1108, https://doi.org/10.1021/jp076981k.
[29] T. Kosec, D.K. Merl, I. Milošev, Impedance and XPS study of benzotriazole films formed on copper, copper–zinc alloys and zinc in chloride solution, Corros. Sci. 50 (2008) 1987–1997, https://doi.org/10.1016/j.corsci.2008.04.016.
[30] J. Olsson, S.L.S. Stipp, K.N. Dalby, S.R. Gislason, Rapid release of metal salts and nutrients from the 2011 Grímsvötn, Iceland volcanic ash, Geochim. Cosmochim. Acta 123 (2013) 134–149. doi:https://doi.org/10.1016/j.gca.2013.09.009.
[31] V.P. Zakaznova-Herzog, H.W. Nesbitt, G.M. Bancroft, J.S. Tse, Characterization of leached layers on olivine and pyroxenes using high-resolution XPS and density functional calculations, Geochim. Cosmochim. Acta 72 (2008) 69–86, https://doi.org/10.1016/j.gca.2007.09.031.
[32] E. Enríquez, V. Fuertes, M.J. Cabrera, J. Seores, D. Muñoz, B. Galiana, J. F. Fernández, Study of the crystallization in fast sintered Na-rich plagioclase glass-ceramic, Ceram. Int. 45 (2019) 8899–8907, https://doi.org/10.1016/j.ceramint.2019.01.219.
[33] T.J. Šarapatka, XPS study of light-induced effects on Pd-Si and Pd-SiO2-Si interfaces, J. Electron Spectros. Relat. Phenomena. 58 (1992) 233–245, https://doi.org/10.1016/0368-2048(92)80022-Z.
[34] J.E. Gittens, T.J. Smith, R. Suleiman, R. Akid, Current and emerging environmentally-friendly systems for fouling control in the marine environment, Biotechnol. Adv. 31 (2013) 1738–1753, https://doi.org/10.1016/j.biotechadv.2013.09.002.
[35] W.J. Yang, K.G. Neoh, E.T. Kang, S.L.M. Teo, D. Rittschof, Polymer brush coatings for combating marine biofouling, Prog. Polym. Sci. 39 (2014) 1017–1042, https://doi.org/10.1016/j.progpolymsci.2014.02.002.
[36] Q. Xie, J. Pan, C. Ma, G. Zhang, Dynamic surface antifouling: mechanism and systems, Soft Matter 15 (2019) 1087–1107, https://doi.org/10.1039/c8sm01853g.
[37] G. Zhang, J. Liu, Y. Zhu, T. Shen, D. Quan Yang, Enhanced antibacterial efficacies, corrosion resistance, and cytocompatibility of ZnO/CuO composite coatings through designed sputtering orders, Appl. Surf. Sci. 635 (2023) 157724, https://doi.org/10.1016/j.apsusc.2023.157724.
[38] A. Kraš, I. Milošev, The aqueous chemistry of zirconium as a basis for better understanding the formation of zirconium conversion coatings: updated thermodynamic data, J. Electrochem. Soc. 170 (2023) 021508, https://doi.org/10.1149/1945-7111/acb9c2.
[39] S. Calderon Velasco, A. Cavaleiro, S. Carvalho, Functional properties of ceramic-Ag nanocomposite coatings produced by magnetron sputtering, Prog. Mater. Sci. 84 (2016) 158–191, https://doi.org/10.1016/j.pmatsci.2016.09.005.
[40] M.S. Islam, A. Aryasomayajula, P.R. Selvaganapathy, A review on macroscale and microscale cell lysis methods, Micromachines 8 (2017), https://doi.org/10.3390/mi8030083.
[41] Y. Shen, Z. Liu, Y. Kong, X. Wang, J. Li, H. Ning, C. Pan, Effect of Cr content on micro-galvanic dissolution behavior and corrosion characteristics of cu-Cr alloy laser cladding layer in a simulated seawater environment, Appl. Surf. Sci. 647 (2024) 158972, https://doi.org/10.1016/j.apsusc.2023.158972.
[42] Woods Hole Oceanographic Institution, Marine Fouling and its Prevention, Annapolis, Maryland, 1952 https://www.vliz.be/imisdocs/publications/224762.pdf.
[43] E. Ytreberg, K. Hansson, A.L. Hermansson, R. Parsmo, M. Lagerström, J.-P. Jalkanen, I.-M. Hassellöv, Metal and PAH loads from ships and boats, relative other sources, in the Baltic Sea, Mar. Pollut. Bull. 182 (2022) 113904, https://doi.org/10.1016/j.marpolbul.2022.113904.
[44] Directorate-General for Environment, Baltic Sea shipping should avoid copper in antifouling paints and open-loop scrubbers to mitigate pollution, in: EU Environ. Newsl., "Science for Environment Policy", 2023. Issue 600, https://environment.ec.europa.eu/news/baltic-sea-shipping-should-avoid-copper-antifouling-paints-and-open-loop-scrubbers-mitigate-2023-05-24_en. (Accessed 9 August 2024).